ASME Journal of Micro and Nano Science and Engineering
Online journal at:
https://asmedigitalcollection.asme.org/micronanomanufacturing

Karson Wardell
Department of Mechanical Engineering,
University of Mississippi,
Oxford, MS 38677
e-mail: kdwardel@go.olemiss.edu

Yao Yao
Department of Industrial and Systems Engineering,
University of Missouri,
Columbia, MO 65211
e-mail: yytk7@missouri.edu

Qingrui Jiang
Department of Mechanical Engineering,
University of Mississippi,
Oxford, MS 38677
e-mail: qjiang1@go.olemiss.edu

Shinghua Ding
Department of Chemical and Biomedical Engineering,
University of Missouri,
Columbia, MO 65211
e-mail: dings@missouri.edu

Yi Wang[1]
Department of Industrial and Systems Engineering,
University of Missouri,
Columbia, MO 65211
e-mail: yiwang@missouri.edu

Yiwei Han[1]
Department of Mechanical Engineering,
University of Mississippi,
Oxford, MS 38677
e-mail: yhan2@olemiss.edu

Direct Printing of High-Resolution Metallic Three-Dimensional Microneedle Arrays Via Electrohydrodynamic Jet Printing

Three-dimensional (3D) microneedle arrays (MAs) have shown remarkable performances for a wide range of biomedical applications. Achieving advanced customizable 3D MAs for personalized research and treatment remain a formidable challenge. In this paper, we have developed a high-resolution electrohydrodynamic (EHD) 3D printing process for fabricating customizable 3D MAs with economical and biocompatible molten alloy. The critical printing parameters (i.e., voltage and pressure) on the printing process for both two-dimensional (2D) and 3D features are characterized, and an optimal set of printing parameters was obtained for printing 3D MAs. We have also studied the effect of the tip-nozzle separation speed on the final tip dimension, which will directly influence MAs' insertion performance and functions. With the optimal process parameters, we successfully EHD printed customizable 3D MAs with varying spacing distances and shank heights. A 3 × 3 customized 3D MAs configuration with various heights ranging from 0.8 mm to 1 mm and a spacing distance as small as 350 μm were successfully fabricated, in which the diameter of each individual microneedle was as small as 100 μm. A series of tests were conducted to evaluate the printed 3D MAs. The experimental results demonstrated that the printed 3D MAs exhibit good mechanical strength for implanting and good electrical properties for electrophysiological sensing and stimulation. All results show the potential applications of the EHD printing technique in fabricating cost-effective, customizable, high-performance MAs for biomedical applications. [DOI: 10.1115/1.4065965]

1 Introduction

Three-dimensional (3D) microneedle arrays (MAs) have shown outstanding performance in drug delivery, electrophysiological recording and stimulation, biochemical sensing, etc., Refs. [1–4]. Researchers have reported various MAs with different designs, such as diameters, heights, tip geometries, and densities, for a wide range of biomedical applications. For example, MAs are one of the most promising transdermal drug delivery components, which show high delivery efficiency of drugs, vaccines, proteins, and nanoparticles with a minimally invasive nature [5,6]. On the other hand, advancing bio-electric acquisition technology allows the use of 3D MAs for wearable biopotential monitoring and stimulation [1,7]. As the spiky tips of MAs can penetrate the stratum corneum with minimally invasive, MAs can be used as dry electrodes without conductive gel for long-term high-signal-quality electrophysiological monitoring [8]. In addition, MAs can be adopted as implantable 3D neural micro-electrode arrays, which provide neuroscientists with promising means to investigate the nervous system dynamics for deciphering the functional connections among regions of the brain and understanding the mechanism of brain dysfunction [9–11]. Overall, 3D MAs display massive potential for various advanced bio-electronics applications.

Various manufacturing methods have been reported to fabricate MAs using silicon, metal, and polymers [7,12,13]. Photolithography with subsequent etching techniques is commonly employed to fabricate silicon-based MAs on the wafer [14,15]. Although microelectromechanical systems (MEMS) technologies enable high-resolution fabrication, they inevitably rely on sophisticated equipment and complicated procedures [16]. The MEMS

Manufacturing Science and Engineering Conference, June 17–21, 2024.
[1]Corresponding authors.
Contributed by the Manufacturing Engineering Division of ASME for publication in the Journal of Micro and Nano Science and Engineering. Manuscript received March 27, 2024; final manuscript received July 5, 2024; published online October 9, 2024. Assoc. Editor: Sylvie Castagne.

technologies also limit the customizability and aspect ratio (height/diameter) of the fabricated MAs. Moreover, silicon is a brittle material, and the silicon-based MAs are subjected to breakage during the handling and insertion process [17]. Several methods are also reported for fabricating metal MAs, such as computer numerical control micromachining [18–20], laser cutting [21], wire-electrode cutting [22], and electrochemical etching [23]. Compared with MEMS technology, these methods have potential customizability, while they are relatively low in accuracy and high in cost due to their subtractive processing nature. Most of the time, these methods are difficult to be applied for mass production. Polymer MAs also show great potential for various types of MAs. As the polymer has a relatively low melting point, it can be manufactured using micromolding [24], thermal drawing [25], and droplet-born air blowing [26]. Although the micromolding of polymer MAs is able to be mass-produced, fabricating the master mold for the micromolding is still challenging and expensive.

Currently, researchers are pursuing a smaller footprint with a higher density and aspect ratio to allow higher spatial resolution of MAs. For example, the Utah micro-electrode array, widely used for neurological applications, has a spatial resolution of 400 μm, while the aspect ratio is only about 15, which is difficult to use for deep brain stimulation [27]. Importantly, to meet the needs of precision healthcare and treatment, customized MAs (customized individual needle dimensions, geometry, and overall layout) are also an urgent need. Unfortunately, the currently reported fabrication methods are still struggling to achieve the aforementioned requirements.

Three-dimensional printing is a powerful tool that has attracted a lot of interest due to its excellent fabrication capability, flexible design, minimized waste, and cost-effectiveness [28,29]. It has the capability of rapid prototyping and customized production of parts for different applications (e.g., automotive, healthcare, aerospace, electronics, etc.) [30]. Ink-based 3D printing has already been used to fabricate electrodes for various purposes (e.g., energy storage units, supercapacitors, healthcare, etc.) [31–34]. Despite the rapid development of ink-based 3D printing applications, direct printing of 3D MAs has rarely been explored. Most traditional 3D printing techniques are reported to fabricate 3D structures using polymer [35], metallic powders [36], and nanoparticles [37]. However, they are limited by the printing resolution and materials, making them difficult to employ for high-density and high aspect ratio MAs fabrication. Electrohydrodynamic (EHD) jet printing [38] is a cost-effective and high-resolution printing technique that can be applied to various functional materials, such as polymers [39], nanoparticles [40], molten alloys [41], etc. It has been proven to be an effective method to fabricate conductive metallic features such as electrodes and conductive traces [42]. Compared with conductive nanomaterials (e.g., silver nanoparticles, carbon nanotubes, etc.), molten alloy is a convenient and affordable material option for printing conductive features without any postprocessing, such as sintering or curing. Currently, research on the EHD printing of molten alloys primarily focuses on printing two-dimensional (2D) patterns [41]. Only a few groups have investigated the EHD printing capability of 3D metallic structures for electronics with molten alloys. Ren's group has printed vertical interconnect accesses for vertical interconnects, but each single printed vertical interconnect access acted as an access point, which was very challenging to use as an electrode array [43]. A cost-effective process still needs to be developed to fabricate high-density, high aspect ratio, and customizable 3D MAs, which can be further applied for various biomedical applications.

In this paper, we present an agile manufacturing method enabled by the EHD printing process to produce high-density, high aspect ratio, and customizable 3D MAs by direct printing of molten alloys. By optimizing a series of printing parameters, 3×3 3D MAs with customized shank heights (from 0.8 to 2 mm) and layouts (spacing as small as 350 μm) are successfully printed. The effects of the nozzle-tip separation speed on the tip geometry are also studied, which provides a guideline for fabricating optimized microneedle tips for minimized tissue damage in the future. Moreover, the mechanical and electrical properties of printed 3D MAs have been characterized. Compared with the current MEMS manufacturing approaches, EHD printing can significantly reduce the fabrication complexity and cost for customized 3D MAs while providing better performance and higher dimensional accuracy.

2 Materials and Methods

2.1 Electrohydrodynamic Printing System and Printing Material. Figure 1 illustrates an EHD printing system that consists of four major components: a high-voltage supply (Trek 610E, Lockport, NY), a pneumatic dispensing system, a heating system, and a precision three-axis motion stage (PI-USA, Hopkinton, MA). In EHD printing, a high electric voltage is applied between the printing nozzle and the ground under the substrate to form a Taylor-cone structure, and a fine jet or droplet will be ejected from the apex of the cone. The produced jet or droplet can be much smaller than the nozzle size, which overcomes the nozzle size limitation and nozzle clogging. The pneumatic dispensing syringe provides controllable pressure for the ink to assist its flow. The syringe can be heated by a proportional-integral-derivative-controlled heating component, in which temperature is measured by a high-precision thermocouple. The precision motion stage is adopted to control the motion of the printhead and substrate in the *XYZ* axis with an accuracy and repeatability of less than 50 nm. All the printing processes are program-controlled on the computer and sent to the motion system. A camera with a resolution of 1.6 μm is used to monitor the printing process. The nozzle is selected with an outer diameter of 251 μm and an orifice of 160 μm. The material used in this study is Field's Metal (32.5% Bismuth, 51% Indium, 16.5% Tin) ingot, which is a eutectic alloy with a melting point of 62 °C. Kalantar-Zadeh's work has demonstrated a good biocompatibility of field's metal, which makes this material a good candidate for fabricating 3D MAs for various bio-applications [44].

2.2 Electrohydrodynamic Printing Process Characterization. The printing temperature of the metal ink was set to 70 °C, which was just above its melting point. Higher printing temperatures will lead to a longer time for the printed electrodes to get solidified, reducing the resolution of the features and increasing the difficulties during the printing. The ink was first characterized on the 2D plane to obtain the optimal printing parameters for conductive traces, which will be connected with external circuits. Printing voltage and pressure are identified as two critical printing parameters that directly affect the printing behavior and resolution. Experiments have been conducted at least five times to characterize each parameter, and we have selected five points to measure printed feature diameters. We will select the parameters that can achieve the

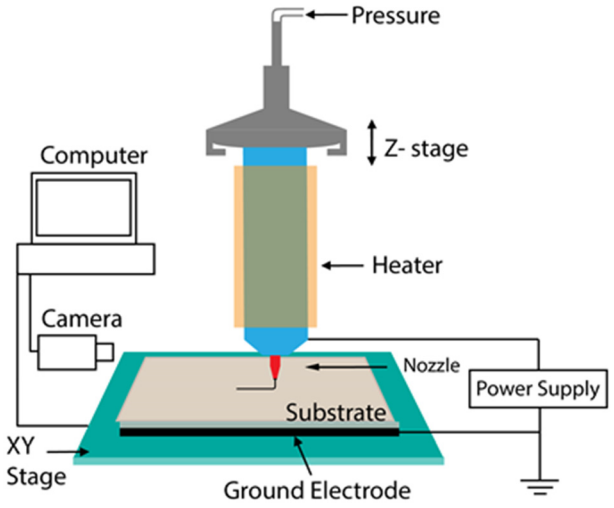

Fig. 1 Schematic of EHD printing system

most uniform and best resolution as the optimal value. The printing speed for 2D features was kept at a constant of 0.25 mm/s. The optimal parameters obtained from the test were used to print conductive traces and served as the reference for the printing of 3D MAs.

The 3D MAs can be directly printed right after printing connecting traces by lifting the Z axis. The interaction among the applied electric field, pressure, and nozzle lifting speed influences the EHD printability of the 3D MAs. According to our studies, a higher lifting speed will make the printing process more vulnerable to disturbance, while a lower lifting speed will dramatically reduce the resolution of the shank as more materials will be carried out. In this paper, the lifting speed was kept at a constant of 0.15 mm/s for stable printing. To characterize the printing voltage and pressure, one parameter was kept constant, and the other parameter was changed gradually. The printed shanks of 3D MAs were observed and characterized under the camera and optical microscope. The pressure was first selected from 0 to 1 psi, and the applied voltage was maintained at 1.5 kV. Then, we kept a constant pressure of 0.5 psi and changed the voltage from 0 to 1.5 kV. A feasible set of printing parameters was finally obtained after the characterization.

Tip geometry is critical for sensing signals and insertion performance. The separation speed between the nozzle and needle was also investigated to study the formation of the needle tip. This speed directly affects the geometry of the needle tip during tip formation. A longer separation time will increase the length of the tip, enabling a sharper tip and vice versa. In the characterization of the tip formation process, the voltage and pressure were removed from the printing system to reduce the ink flowrate, and only the separation speed was applied to form the tip, ensuring a robust needle tip for implantable device applications. The separation speeds were investigated from 5 mm/s to 13 mm/s with an interval of 2 mm/s. Table 1 summarizes the printing parameters used in the experiments.

2.3 Fabrication of Customizable Three-Dimensional Microneedle Arrays. The customized MAs and associated connection traces were designed in the computer using CAD software and transferred to the stage controlling software. The 2×2 and 3×3 3D arrays were then printed with the optimal printing parameters determined from above. MAs with different spacing distances (1 mm, 500 μm to 350 μm) are designed for the printing. The spacing of 350 μm is smaller than the spacing (400 μm) in the Utah array fabricated by MEMS technology. To further test the printing capability and customizability of EHD printing technology for MAs, shanks with varying heights (from 0.8 mm to 2 mm) in each microneedle were also printed.

2.4 Characterization of Printed Three-Dimensional Microneedle Arrays

2.4.1 Mechanical Properties Characterization. The mechanical properties of printed MAs are first characterized based on a tensile testing experiment. A dynamic mechanical analyzer DMA7100 (Hitachi®, Hillsboro, OR) was employed to exert a constant pulling speed at 15 μm/s, while recording the associated force at room temperature (20 °C). The printed single microneedle was fixed on a pair of laser-cut acrylic boards using epoxy glue to hold on to the tester, ensuring a firm grip and minimizing the chances of slippage. The diameter and effective length of the microneedle were measured using a microscope before the tensile test. According to the measurement results, the engineering strain–stress curve can be plotted, and Young's modulus can be estimated based on the slope in the linear portion (elastic region) of the strain–stress curve.

To test the implantability of MAs, agarose phantom tissue was used in this research, which can possess similar mechanical properties to animal tissue by controlling the weight percentage of agarose powder, such as brain tissue (0.4–0.6 wt.%). We prepared the agarose phantom tissue by dissolving the agarose powder (Biotech®, Knoxville, TN) in a phosphate buffer solution (PBS) (Sigma Aldrich®, St. Louis, MO) with a concentration of 0.6 wt.%. An agarose gel concentration of 0.6 wt.% was identified as accurately mimicking the properties of the mammalian brain [45]. This mixture was heated in a microwave for 30 s and then transferred to a small mold for cooling down and solidification. During the MA insertion, we utilized a camera to monitor any bending or deflection in the transparent agarose phantom tissue.

2.4.2 Electrical Properties Characterization. The Field's metal ingot possesses excellent electrical conductivity. In this paper, an ohmmeter (Fluke® 45, Everett, WA) was used to measure the resistance of printed lines on glass slides. The dimensions and cross-sectional areas of the samples were measured using an optical profilometer (Vecco® NT 9109, Plainview, NY). The resistivity of the printed Field's metal is calculated based on the following equation:

$$\rho = \frac{AR}{l} \tag{1}$$

where ρ is the resistivity, l is the length, A is the cross-sectional area, and R is the measured resistance.

To examine the potential of utilizing printed MAs for electrophysiological measurement, the printed MAs were used as electrodes for the signal measurements. In the paper, simplified recording experiments were performed using printed MAs in PBS solution to mimic the electrophysiology experiment. The fabricated MAs were connected to an oscilloscope, and a pure copper wire was connected to the signal generator. All the electrodes and copper wire were immersed in a PBS solution. When a sinusoidal signal was emitted from the copper wire, the oscilloscope will display a corresponding signal received from MAs in another site.

3 Results and Discussion

3.1 Printing Results. In this study, we find that both dispensing pressure and voltage affect printing performance for 2D patterns and 3D structures. Figure 2(*a*) shows the relationship between the dispensing pressure and printing performance under a constant voltage of 1.5 kV, printed on a 2D plane. Due to the large surface tension of the Field's metal ink, only applying a high electric field

Table 1 Printing parameters of experiment setting

Two-dimensional printing		Three-dimensional printing		Tip formation
Voltage (kV)	Pressure (psi)	Voltage (kV)	Pressure (psi)	Separation speed (mm/s)
1.5	0	1.5	0	5
1.5	0.25	1.5	0.25	7
1.5	0.5	1.5	0.5	9
1.5	1	1.5	1	11
0	0.5	0	0.5	13
1.5	0.5	0.75	0.5	—
1.75	0.5	1.5	0.5	—
2	0.5	2.25	0.5	—

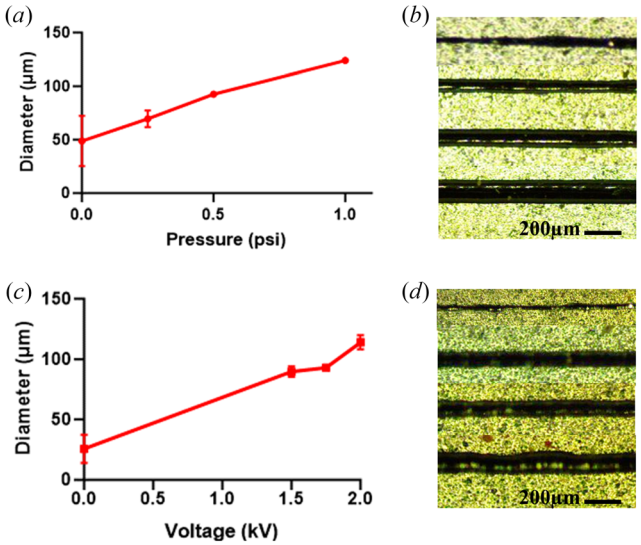

Fig. 2 (*a*) and (*b*) Printed metallic filament under different pressures (0 psi, 0.25 psi, 0.5 psi, 1 psi) with a constant voltage of 1.5 kV. The diameters were measured from top to bottom; (*c*) and (*d*) printed metallic filament under different voltages (0 V, 1.5 kV, 1.75 kV, 2 kV) with a constant pressure of 0.5 psi. The diameters were measured from top to bottom. Each experiment has been repeated at least five times to ensure the accuracy. Due to the very small variances of printed filament under 0.5 psi and 1 psi, the error bars are not visible in the figures.

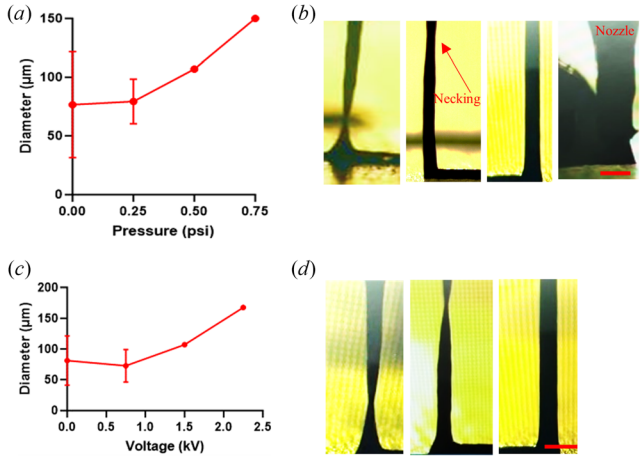

Fig. 3 (*a*) Relation between the printed microneedle diameter and applied pressure with a constant voltage of 1.5 kV, (*b*) camera images of printed microneedle under different pressures (from left to right: 0 psi, 0.25 psi, 0.5 psi, 1 psi) with a constant voltage of 1.5 kV, (*c*) relation between the printed microneedle diameter and applied voltage with a constant pressure of 0.5 psi, and (*d*) camera images of printed microneedle under different voltages (from left to right: 0 V, 0.75 kV, 1.5 kV) with a constant pressure of 0.5 psi. Each experiment has been repeated at least five times to ensure the accuracy. Due to the very small variances of printed filament under 0.5 psi, 1 psi, 1.5 kV, and 2.25 kV, the error bars are not visible in the figures. Scale bar: 200 μm.

cannot provide a sufficient driving force to pull the metal ink out from the printing nozzle. Due to the insufficiency of the ink flow, a small volume of ink is printed on the substrate, as shown in the first line at the top of Fig. 2(*b*). When the pressure is increased to 0.25 psi, a continuous nonuniform line starts to be printed. Continuously increasing the pressure to 0.5 psi, a uniform metal line with a diameter of 92.6±0.8 μm can be achieved. Further increasing the pressure to 1 psi, the diameter of the metal line will increase to 123.8±1.0 μm. It can be explained that higher pressure increases the ink flow, thereby increasing the diameter of the printed ink. However, this trend will stop when there is a mismatch between the printing speed and high ink flow. A large droplet will accumulate around the nozzle tip when the pressure exceeds 1.5 psi. On the other hand, when keeping a constant pressure of 0.5 psi, printed features under different voltages are also tested, as shown in Figs. 2(*c*) and 2(*d*). A very small amount of materials can be observed on the substrate with zero voltage. After increasing the voltage to 1.5 kV, a finer diameter of less than 90 μm metallic line can be successfully printed. A higher voltage (e.g., 2.0 kV) results in a larger average diameter (115 μm). The inherent reason is that higher voltages generate higher electrostatic forces, which leads to dispensing more material, resulting in larger printing diameters.

Figures 3(*a*) and 3(*b*) show the printed shanks of 3D MAs under different pressures while keeping the same voltage. Although the high electric field can extract a small volume of metal ink out of the nozzle without pressure, it cannot provide continuous ink flow at the nozzle tip, and the MA is very easy to break during printing, limiting the printed height of the MA. The left image of Fig. 3(*b*) shows the fractured moment for a short MA when no pressure is applied. At the fractured moment, a necking phenomenon similar to the necking in the tensile test can be observed, which is the mechanism to form a sharp tip for MA. When the pressure is increased to 0.25 psi, more materials can be carried out, resulting in a longer MA, which is shown in the second image from the left of Fig. 3(*b*). However, it is still insufficient for the EHD printing system to produce a high aspect ratio MA, and necking is observed during the printing. This is because the electrostatic force decreases as the nozzle height increases. Initially, the electrostatic force and pressure can dispense enough materials, but by lifting the nozzle, the reduced electrostatic force will bring less materials, thus creating the necking. Further increasing the pressure to 0.5 psi, the system can produce the electrode continuously without breaking (the second right image of Fig. 3(*b*)). In this printing condition, the MA with 2 mm in height and 107.0±1.2 μm in diameter can be achieved with excellent uniformity. After applying a higher pressure of 1 psi, a large droplet is formed at the nozzle tip due to a vast pressure force, making the printing process uncontrollable (the right image of Fig. 3(*b*)). Similar to the pressure, the voltage can also control the ink flow rate. A higher voltage will provide a higher electrostatic force that will increase the amount of material ejected from the nozzle. It is a balance of selecting the voltage and pressure to achieve successful printing. Figures 3(*c*) and 3(*d*) show the different printing results with varied printing voltages. A break is observed when applying a 0 V voltage and lifting the nozzle on the z-axis due to insufficient electrostatic force. Increasing voltage to 0.75 kV, a higher microneedle can be obtained with a limited shank height. This can also be explained by the fact that increasing the nozzle-substrate distance will reduce the electric field strength, thus reducing the electrostatic force. Further increasing the voltage to 1.5 kV, a microneedle with a uniform diameter of 108.3±1.0 μm can be achieved. Continuously increasing the voltage will result in microneedles with larger diameters (167.7±1.3 μm) due to the increased ink flowrate.

The tip geometry and dimension also play a critical role for MAs in medical applications or bio-electronics. When the MAs are used for the 3D micro-electrodes, the tip geometry will directly determine the sensing sensitivity, response time, and signal quality [27,46]. On the other hand, the tip shape and size of the MAs also affect tissue penetration performance and damage [46]. Figures 4(*a*)–4(*f*) show the optical and scanning electron microscopy (SEM) images of the formed tips under different separation speeds from 5 mm/s to 13 mm/s. Figure 4(*g*) shows the plot of the relation between the printing speed and measured tip length. The tip formation is based on the fracture during the separation of the tip and nozzle. When applying a lower separation speed (e.g., 5 mm/s), the tip was longer than the tip fabricated under a higher separation (e.g., 9 mm/s). This can be explained by the fact that a lower separation speed will have a

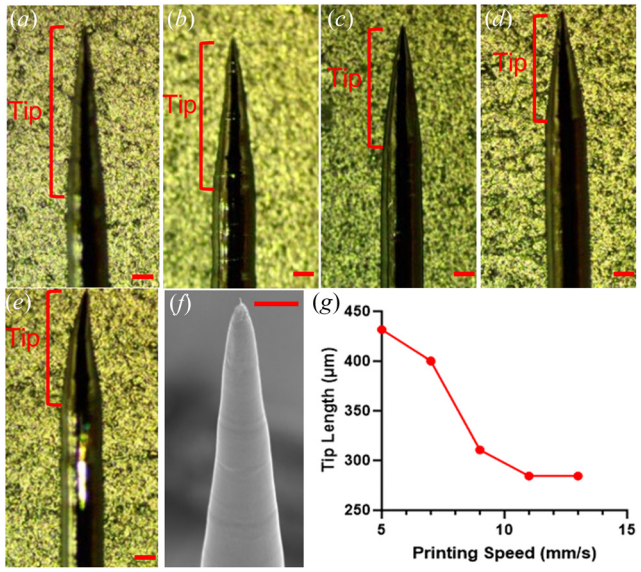

Fig. 4 (*a*)–(*e*): Optical image of printed tips with different separation speeds (from left to right: 5 mm/s, 7 mm/s, 9 mm/s, 11 mm/s, and 13 mm/s), (*f*) SEM image of printed tip apex with a 5 mm/s separation speed, and (*g*) relation between the printing speeds and tip lengths. Each experiment has been repeated at least five times to ensure the accuracy. Scale bar: 50 μm.

lower strain rate, which allows the material to have more time to reform, thus forming a longer tip. Moreover, a lower separation speed takes longer to cause the break, which allows more materials to be carried out, contributing to a longer tip. In addition, the shape of the apex at the tip was also affected by the separation speed. A relatively low separation speed will create a straight tip, while a higher speed will create bent tips, which are shown in Fig. 4(*d*). Moreover, a much higher separation speed will bend tips with a larger bending radius (Fig. 4(*e*)). This may be due to the vibration, turbulence, and solidification time during the separation process.

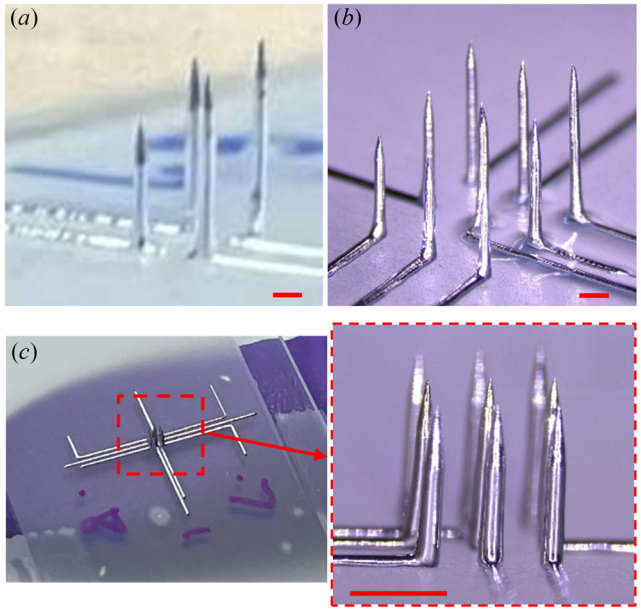

Fig. 5 (*a*)–(*c*) EHD printed MAs with different spacing and shank heights: (*a*) A 2 × 2 MAs with different shank heights (spacing: 1 mm), (*b*) a 3 × 3 MAs with different shank heights (spacing size: 1 mm), and (*c*) a 3 × 3 MAs with different shank heights (spacing size: 350 μm) was placed on the finger. Each experiment has been repeated at least five times. Scale bar: 500 μm.

Higher separation speed will cause larger vibration and shorter solidification time, which causes some turbulences on the tip. To achieve a stable printing process and best printed electrode, the separation speed was selected as 5 mm/s, and Fig. 4(*f*) shows the SEM image of the printed tip. The diameter of the apex of the printed tip is less than 5 μm, which has the potential to be used for cell penetration.

Based on the above process experiments, the optimal printing parameters are selected as printing voltage: 1.5 kV; pressure: 0.5 psi; separation printing speed: 9 mm/s. With the optimized printing parameters, 3D MAs with customized shank heights and spacing were successfully printed via EHD printing technology. 2 × 2 and 3 × 3 MAs with spacing of 350 μm can be achieved. Figures 5(*a*) and 5(*b*) show printed 2 × 2 and 3 × 3 MAs with a spacing distance of 1 mm and shank heights ranging from 1 mm to 2 mm. Figure 5(*c*) is a 3 × 3 MA placed on the finger with a spacing of only 350 μm, which was narrower than the reported Utah array fabricated by MEMS technology. Importantly, the average printing time for each individual microneedle is only about 10 s, and the total time needed for printing each 3 × 3 MA is less than 2 min, which is much faster than conventional machining methods. The samples demonstrate the great potential of applying EHD printing to fabricate customized high-density MAs for various biomedical applications. With the small spacing distance, the shank with different heights (from 0.8 mm to 1 mm) can still be fabricated. The diameter for all printed MAs was about 100 μm. The resolution can be further improved by employing nozzles with smaller orifices, which further improves the density.

3.2 Characterization Results of Printed Microneedle Arrays. Young's module of the printed MAs is measured and calculated based on its strain–stress curve, as shown in Fig. 6(*a*). The calculated slope of the stain–stress curve in the elastic region is about 3.15 GPa. Compared to Young's module of silicon

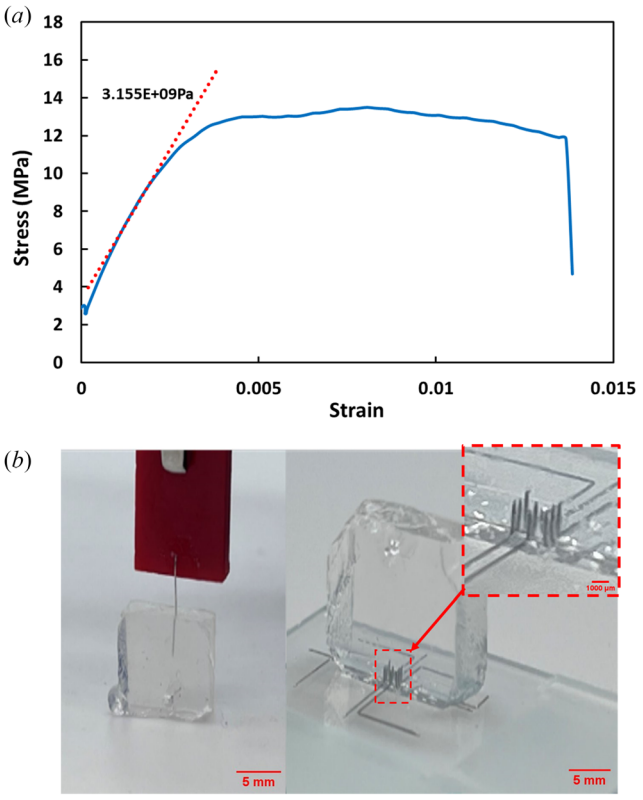

Fig. 6 (*a*) Tensile test of printed microneedle. This test has been repeated three times to ensure an accurate result. (*b*) Photo of implantation of MAs in phantom tissue.

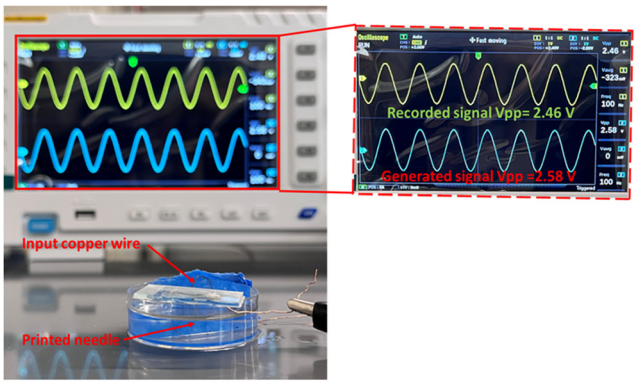

Fig. 7 Experiment setup with printed microneedle. This experiment has been repeated five times to ensure the accuracy.

(130–187 GPa), the smaller Young's module of Field's metal indicates the printed MAs are more flexible than traditional silicon-based MAs, which can further reduce potential tissue damage and inflammation.

To successfully implant the MAs, critical buckling load governs the insertion of MAs into the tissue, as shown in the following equation:

$$F_{\text{buckling}} = \frac{\pi^2 \text{EI}}{(KL)^2} \tag{2}$$

where E is Young's modulus, I is the second moment of the microneedle, L is the unsupported length of the microneedle, and K is the length factor (0.5–1). As Young's modulus of our printed MAs has been characterized in the tensile test, the critical force of various sizes of printed microneedle can be estimated based on the critical buckling equation, where a success penetration requires the buckling force to be greater than the force applied for the insertion. Figure 6(*b*) shows that a microneedle with an aspect ratio of over 100 and an MA were successfully inserted into phantom tissue with 0.6 wt.% agarose without bending or failure. This result shows the potential of applying high-aspect ratio MAs for various biomedical applications, such as neural interfaces.

By measuring the resistance and cross-sectional area of the printed features, the averaged resistivity of the printed Field's metal can be calculated as $2.096 \pm 0.215\ \mu\Omega\cdot$m with five measurements, which is about 1×10^{-9} of that of silicon-based electrodes. The excellent electrical conductivity of the printed microneedle makes it a good candidate for use as a micro-electrode in electrophysiology sensing and stimulation. Figure 7 shows an experiment where the printed microneedle was used to sense the signal generated in the PBS solution with a *p*H of 7.4. The microneedle can successfully record the signal with little losses (input voltage 2.58 V and output voltage 2.46 V). Therefore, the printed MAs hold great potential for micro-electrode arrays for electrophysiology sensing and stimulation. For future bio-applications, a gold or PEDOT:PSS coating can be electroplated to further improve biocompatibility and conductivity.

4 Conclusion

This paper presents a novel, cost-effective manufacturing approach for the direct fabricating of 3D MAs with high-resolution EHD printing. The effect of the critical printing parameters, including pressures, EHD printing voltages, and printing speeds, on the printability, printing process, and resolution of the 3D MAs were characterized. With EHD printing, the electrostatic force can continuously eject molten alloy ink to produce 3D MAs with high resolution and small spacing. In this paper, we have successfully achieved 3D MAs with around 100 μm shank diameter, customized shank height, and spacing size as small as 350 μm, which is smaller than the spacing of the Utah array fabricated by MEMS technology. More importantly, the results of mechanical and electrical tests of printed MAs demonstrate excellent performance in implantation and signal collection. All results show the potential of utilizing the EHD printing technique to fabricate high-density, high-aspect-ratio customizable MAs for various biomedical applications.

Funding Data

- National Science Foundation (NSF), Division of Integrative Organismal Systems (Award No. IOS-2200200; Funder ID: 10.13039/100000154).

Data Availability Statement

The datasets generated and supporting the findings of this article are obtainable from the corresponding author upon reasonable request.

References

[1] Li, J., Ma, Y., Huang, D., Wang, Z., Zhang, Z., Ren, Y., Hong, M., et al., 2022, "High-Performance Flexible Microneedle Array as a Low-Impedance Surface Biopotential Dry Electrode for Wearable Electrophysiological Recording and Polysomnography," Nano-Micro Lett., **14**(1), p. 132.
[2] Li, R., Zhang, L., Jiang, X., Li, L., Wu, S., Yuan, X., Cheng, H., Jiang, X., and Gou, M., 2022, "3D-Printed Microneedle Arrays for Drug Delivery," J. Controlled Release, **350**, pp. 933–948.
[3] Barnum, L., Quint, J., Derakhshandeh, H., Samandari, M., Aghabaglou, F., Farzin, A., Abbasi, L., Bencherif, S., Memic, A., Mostafalu, P., and Tamayol, A., 2021, "3D-Printed Hydrogel-Filled Microneedle Arrays," Adv. Healthcare Mater., **10**(13), p. 2001922.
[4] Sarabi, M. R., Bediz, B., Falo, L. D., Korkmaz, E., and Tasoglu, S., 2021, "3D Printing of Microneedle Arrays: Challenges Towards Clinical Translation," J. 3D Print. Med., **5**(2), pp. 65–70.
[5] Vora, L. K., Moffatt, K., Tekko, I. A., Paredes, A. J., Volpe-Zanutto, F., Mishra, D., Peng, K., Raj Singh Thakur, R., and Donnelly, R. F., 2021, "Microneedle Array Systems for Long-Acting Drug Delivery," Eur. J. Pharm. Biopharm., **159**, pp. 44–76.
[6] Halder, J., Gupta, S., Kumari, R., Gupta, G. D., and Rai, V. K., 2021, "Microneedle Array: Applications, Recent Advances, and Clinical Pertinence in Transdermal Drug Delivery," J. Pharm. Innovation, **16**(3), pp. 558–565.
[7] Wang, R., Bai, J., Zhu, X., Li, Z., Cheng, L., Zhang, G., and Zhang, W., 2022, "A PDMS-Based Microneedle Array Electrode for Long-Term ECG Recording," Biomed. Microdevices, **24**(3), p. 27.
[8] Ren, L., Liu, B., Zhou, W., and Jiang, L., 2020, "A Mini Review of Microneedle Array Electrode for Bio-Signal Recording: A Review," IEEE Sens. J., **20**(2), pp. 577–590.
[9] Hoogerwerf, A. C., and Wise, K. D., 1994, "A Three-Dimensional Microelectrode Array for Chronic Neural Recording," IEEE Trans. Biomed. Eng., **41**(12), pp. 1136–1146.
[10] Shin, H., Jeong, S., Lee, J.-H., Sun, W., Choi, N., and Cho, I.-J., 2021, "3D High-Density Microelectrode Array With Optical Stimulation and Drug Delivery for Investigating Neural Circuit Dynamics," Nat. Commun., **12**(1), p. 492.
[11] Saleh, M. S., Ritchie, S. M., Nicholas, M. A., Gordon, H. L., Hu, C., Jahan, S., Yuan, B., et al., 2022, "CMU Array: A 3D Nanoprinted, Fully Customizable High-Density Microelectrode Array Platform," Sci. Adv., **8**(40), p. eabj4853.
[12] Ji, J., Tay, F. E., Miao, J., and Iliescu, C., 2006, "Microfabricated Silicon Microneedle Array for Transdermal Drug Delivery," J. Phys.: Conf. Ser., **34**, pp. 1127–1131.
[13] Omatsu, T., Chujo, K., Miyamoto, K., Okida, M., Nakamura, K., Aoki, N., and Morita, R., 2010, "Metal Microneedle Fabrication Using Twisted Light With Spin," Opt. Express, **18**(17), pp. 17967–17973.
[14] Wang, J., Wang, H., Lai, L., and Li, Y., 2020, "Preparation of Microneedle Array Mold Based on MEMS Lithography Technology," Micromachines (Basel), **12**(1), p. 23.
[15] Bolton, C. J. W., Howells, O., Blayney, G. J., Eng, P. F., Birchall, J. C., Gualeni, B., Roberts, K., Ashraf, H., and Guy, O. J., 2020, "Hollow Silicon Microneedle Fabrication Using Advanced Plasma Etch Technologies for Applications in Transdermal Drug Delivery," Lab Chip, **20**(15), pp. 2788–2795.
[16] Judy, J. W., 2001, "Microelectromechanical Systems (MEMS): Fabrication, Design and Applications," Smart Mater. Struct., **10**(6), pp. 1115–1134.
[17] Vinayakumar, K. B., Hegde, G. M., Nayak, M. M., Dinesh, N. S., and Rajanna, K., 2014, "Fabrication and Characterization of Gold Coated Hollow Silicon Microneedle Array for Drug Delivery," Microelectron. Eng., **128**, pp. 12–18.
[18] Thanh, H. L., Ta, B. Q., The, H. L., Nguyen, V., Wang, K., and Karlsen, F., 2015, "Low-Cost Fabrication of Hollow Microneedle Arrays Using CNC Machining and UV Lithography," J. Microelectromech. Syst., **24**(5), pp. 1583–1593.
[19] Malek-Khatabi, A., Faraji, Rad, Z., Rad-Malekshahi, M., and Akbarijavar, H., 2023, "Development of Dissolvable Microneedle Patches by CNC Machining and Micromolding for Drug Delivery," Mater. Lett., **330**, p. 133328.
[20] Parker, E. R., Rao, M. P., Turner, K. L., Meinhart, C. D., and MacDonald, N. C., 2007, "Bulk Micromachined Titanium Microneedles," J. Microelectromech. Syst., **16**(2), pp. 289–295.

[21] Albarahmieh, E., AbuAmmouneh, L., Kaddoura, Z., AbuHantash, F., Alkhalidi, B. A., and Al-Halhouli, A., 2019, "Fabrication of Dissolvable Microneedle Patches Using an Innovative Laser-Cut Mould Design to Shortlist Potentially Transungual Delivery Systems: In Vitro Evaluation," AAPS PharmSciTech, **20**(5), p. 215.
[22] Li, J., Zhou, Y., Yang, J., Ye, R., Gao, J., Ren, L., Liu, B., Liang, L., and Jiang, L., 2019, "Fabrication of Gradient Porous Microneedle Array by Modified Hot Embossing for Transdermal Drug Delivery," Mater. Sci. Eng.: C, **96**, pp. 576–582.
[23] Wilke, N., Mulcahy, A., Ye, S.-R., and Morrissey, A., 2005, "Process Optimization and Characterization of Silicon Microneedles Fabricated by Wet Etch Technology," Microelectron. J., **36**(7), pp. 650–656.
[24] Juster, H., Aar, B., and Brouwer, H., 2019, "A Review on Microfabrication of Thermoplastic Polymer-Based Microneedle Arrays," Polym. Eng. Sci., **59**(5), pp. 877–890.
[25] Ren, L., Jiang, Q., Chen, K., Chen, Z., Pan, C., and Jiang, L., 2016, "Fabrication of a Micro-Needle Array Electrode by Thermal Drawing for Bio-Signals Monitoring," Sensors (Basel), **16**(6), p. 908.
[26] Chang, H., Zheng, M., Chew, S. W. T., and Xu, C., 2020, "Advances in the Formulations of Microneedles for Manifold Biomedical Applications," Adv. Mater. Technol., **5**(4), p. 1900552.
[27] Ghane-Motlagh, B., and Sawan, M., 2013, "A Review of Microelectrode Array Technologies: Design and Implementation Challenges," Proceedings of the 2013 2nd International Conference on Advances in Biomedical Engineering, Tripoli, Lebanon, Sept. 11–13, pp. 38–41.
[28] Shahrubudin, N., Lee, T. C., and Ramlan, R., 2019, "An Overview on 3D Printing Technology: Technological, Materials, and Applications," Procedia Manuf., **35**, pp. 1286–1296.
[29] Lipson, H., and Kurman, M., 2013, *Fabricated: The New World of 3D Printing*, John Wiley & Sons, Hoboken, NJ.
[30] Gibson, I., Rosen, D., Stucker, B., and Khorasani, M., 2021, *Additive Manufacturing Technologies*, Springer Nature, Cham, Switzerland.
[31] Zhang, W., Liu, H., Zhang, X., Li, X., Zhang, G., and Cao, P., 2021, "3D Printed Micro-Electrochemical Energy Storage Devices: From Design to Integration," Adv. Funct. Mater., **31**(40), p. 2104909.
[32] Jha, S., Velhal, M., Stewart, W., Amin, V., Wang, E., and Liang, H., 2022, "Additively Manufactured Electrodes for Supercapacitors: A Review," Appl. Mater. Today, **26**, p. 101220.
[33] Cui, Z., Han, Y., Huang, Q., Dong, J., and Zhu, Y., 2018, "Electrohydrodynamic Printing of Silver Nanowires for Flexible and Stretchable Electronics," Nanoscale, **10**(15), pp. 6806–6811.
[34] Khan, S., Ali, S., and Bermak, A., 2019, "Recent Developments in Printing Flexible and Wearable Sensing Electronics for Healthcare Applications," Sensors (Basel), **19**(5), p. 1230.
[35] Xu, W., Jambhulkar, S., Zhu, Y., Ravichandran, D., Kakarla, M., Vernon, B., Lott, D. G., et al., 2021, "3D Printing for Polymer/Particle-Based Processing: A Review," Composites, Part B, **223**, p. 109102.
[36] Gadagi, B., and Lekurwale, R., 2021, "A Review on Advances in 3D Metal Printing," Mater. Today, **45**, pp. 277–283.
[37] Tan, H. W., An, J., Chua, C. K., and Tran, T., 2019, "Metallic Nanoparticle Inks for 3D Printing of Electronics," Adv. Electron. Mater., **5**(5), p. 1800831.
[38] Park, J.-U., Hardy, M., Kang, S. J., Barton, K., Adair, K., Mukhopadhyay, D. K., Lee, C. Y., et al., 2007, "High-Resolution Electrohydrodynamic Jet Printing," Nat. Mater., **6**(10), pp. 782–789.
[39] Han, Y., Wei, C., and Dong, J., 2014, "Super-Resolution Electrohydrodynamic (EHD) 3D Printing of Micro-Structures Using Phase-Change Inks," Manuf. Lett., **2**(4), pp. 96–99.
[40] Kamal, W., Rahman, K., Ahmad, S., Shakeel, M., and Ali, T., 2022, "Electrohydrodynamic Printed Nanoparticle-Based Resistive Temperature Sensor," Flexible Printed Electron., **7**(4), p. 045008.
[41] Han, Y., and Dong, J., 2017, "High-Resolution Direct Printing of Molten-Metal Using Electrohydrodynamic Jet Plotting," Manuf. Lett., **12**, pp. 6–9.
[42] Kwon, H.-J., Hong, J., Nam, S. Y., Choi, H. H., Li, X., Jeong, Y. J., and Kim, S. H., 2021, "Overview of Recent Progress in Electrohydrodynamic Jet Printing in Practical Printed Electronics: Focus on the Variety of Printable Materials for Each Component," Mater. Adv., **2**(17), pp. 5593–5615.
[43] Ren, P., and Dong, J., 2021, "Direct Fabrication of Via Interconnects by Electrohydrodynamic Printing for Multi-Layer 3D Flexible and Stretchable Electronics," Adv. Mater. Technol., **6**(9), p. 2100280.
[44] Abbasi, R., Tang, J., Baharfar, M., Zhang, C., Allioux, F.-M., Zhang, J., Tajik, M., et al., 2022, "Induction Heating for the Removal of Liquid Metal-Based Implant Mimics: A Proof-of-Concept," Appl. Mater. Today, **27**, p. 101459.
[45] Gillies, G. T., Allison, S. W., and Tissue, B. M., 2002, "Positive Pressure Infusion of Fluorescent Nanoparticles as a Probe of the Structure of Brain Phantom Gelatins," Nanotechnology, **13**(4), p. 484.
[46] Ferguson, M., Sharma, D., Ross, D., and Zhao, F., 2019, "A Critical Review of Microelectrode Arrays and Strategies for Improving Neural Interfaces," Adv. Healthcare Mater., **8**(19), p. 1900558.